applied sciences

MDPI

Article

Preliminary Applications of a Solid-State C-Band Weather Radar in Hong Kong for the Monitoring of Intense Convective Weather

Tsz-Ki Lau, Hon Yin Yeung, Tai-Wai Hui, Kai Kwong Lai and Pak-Wai Chan *

Hong Kong Observatory, Hong Kong, China; jackylau@hko.gov.hk (T.-K.L.); hyyeung@hko.gov.hk (H.Y.Y.); dhui@hko.gov.hk (T.-W.H.)

* Correspondence: pwchan@hko.gov.hk

Abstract

A solid-state C-band weather radar has been on a trial run in Hong Kong for around three months for detecting intense convective weather, particularly its features in the atmospheric boundary layer. It serves to supplement the long-range surveillance weather radars working at the mountain tops of Hong Kong, a city with rather hilly terrain. Through a number of case studies, this paper demonstrates the application values of the low-elevation angle scans of this weather radar in two major aspects, namely, construction of a three-dimensional wind field extending down to a height of 1 km above sea level, and detection of hail through comparison with ground reports. The wind field at lower altitudes, which could not be obtained before from the mountain-top weather radars alone, is found to provide timely alerts to squalls associated with rainbands (such as bow echoes) and to monitor orographic precipitation. In a hail event over the Pearl River Estuary, the low-elevation scans of the radar are found to detect the occurrence of hail consistent with ground reports. The estimated maximum hail sizes from this radar are also found to be generally comparable with the limited number of actual observations. With lower power consumption, the solid-state radar is more robust and may be deployed at more locations over Hong Kong, particularly the remote locations such as outlying islands and rural areas. It opens up the possibility of building a network of weather radars to monitor the atmospheric boundary layer conditions associated with intense convective weather in an area with hilly terrain.

Keywords: C-band weather radar; wind field; hail

1. Introduction

For the monitoring of severe weather, the Hong Kong Observatory (HKO) operates a number of weather radars in Hong Kong, including two long-range surveillance S-band weather radars on the mountain tops (at Tai Mo Shan of around 1000 m above sea level, and at Tate's Cairn at about 500 m above sea level), two C-band Terminal Doppler Weather Radars (TDWRs) for microburst detection at the Hong Kong International Airport (HKIA), and two X-band weather radars mainly serving the western part of Hong Kong (one unit serving as backup of TDWRs, and one unit of phased array X-band radar with volume scanning every 1 min only on a trial basis). Due to the complex terrain of the territory, there is significant blockage of the radar beams for the C-band and X-band weather radars and thus, low-level winds are mostly available in the region of HKIA, but not for other parts of Hong Kong.

Check for updates

Academic Editor: Atsushi Mase

Received: 24 April 2026
Revised: 12 June 2026
Accepted: 23 June 2026
Published: 30 June 2026

Copyright: © 2026 by the authors. Licensee MDPI, Basel, Switzerland. This article is an open access article distributed under the terms and conditions of the Creative Commons Attribution (CC BY) license.

In early 2026, a C-band weather radar was set up at Cheung Chau, an outlying island in the southern part of Hong Kong. Apart from the tall mountains (up to around 900 m above sea level) on Lantau Island to the northwest, it basically covers the rest of the territory, particularly the southern part of Hong Kong and the coastal waters to the south of the territory, where intense convective weather may develop over the sea. Shortly after its installation, this C-band radar was found to capture a micro-scale vortex to the west of Hong Kong near Macao, which later moved to the southeast to the offshore waters of Hong Kong, just skirting the territory to bring about intense convective weather. This paper documents some more interesting observations from this C-band radar, with particular emphasis on the applications in two areas:

(a) Located close to the sea level, the low-elevation-angle plan position indicator (PPI) scans from this radar provide wind data in the atmospheric boundary layer (below 1 km or so above sea level) with spatial coverage over the Pearl River Estuary, including Hong Kong; as such, a three-dimensional wind field based on multiple weather radars, as reported previously [1], has been expanded downwards to include winds at a height of 1 km above sea level—the lower level winds could be used to capture (i) squalls that may reach the ground brought about by intense convection, and (ii) orographic effect on the southerly flow, resulting in showers in the windward slopes. The use of single- and multiple-Doppler radar observations for retrieving three-dimensional storm airflow has a long history, including early studies of gust fronts, tornadic storms, boundary-layer flows, and derived dynamical fields [2–6]. Such radar-based analyses have also been applied to heavy rainfall and convective systems in the broader South China and western Pacific pre-summer monsoon region [7].

(b) Observations and alerting of hail—though the S-band weather radars with dual polarization capability could be used to provide earlier alerting of hail, the observed hail was located at least 500 to 1000 m above sea level and may not correspond to the ground observations; with lower-elevation angle PPI scans, the Cheung Chau radar may capture the hail closer to the ground and thus, the hail observation may be more consistent with the hail reports from members of the public. Moreover, an initial attempt is made to estimate the hail size based on the Cheung Chau weather radar and compare that with the ground observations.

2. Technical Specifications of the C-Band Radar at Cheung Chau

The weather radar at Cheung Chau is a C-band solid-state radar with a measurement range of about 300 km. It is located on a small tower on top of the Cheung Chau island with an antenna height of about 85 m above mean sea level. The central operating frequency is around 5.722 GHz. It has dual polarization capability and is equipped with an algorithm to classify the hydrometeors, including the detection of hail. Dual-polarization weather radar has been shown to improve hydrometeor classification and hail identification in operational applications, although performance still depends on radar wavelength, calibration, and the ambient storm environment [8,9].

The radar is configured to perform PPI scans at 10 elevation angles, from 0.8 degrees to 23.0 degrees. Each volume scan takes about 3 min. The most useful scans are the 0.8-degree PPI scan with a range of about 310 km and Nyquist velocity of about 23 m/s, and 1.4-degree PPI scan with a range of about 230 km and Nyquist velocity of about 30 m/s. The solid-state radar is found to consume less electricity and it is more suitable for installation at an outlying island such as Cheung Chau in Hong Kong.

3. Three-Dimensional Wind Retrieval Algorithm

The three-dimensional wind field algorithm is the same as that used by Chan et al. (2025) [1] and is known as the Pythonic Direct Data Assimilation method, the software package of which is available in the public domain [10]. In essence, the methodology is based on three-dimensional variational (3DVAR) analysis achieved through the minimization of a cost function, which is a weighted sum of various cost function terms accounting for the constraints from radial velocities from weather radars, mass continuity, vertical vorticity, radiosonde observation, smoothness, model, and point observation [10–13]. The weights of these cost function terms are adjustable parameters reflecting the relative importance of individual constraints. To emphasize the importance of the observed radial velocities, only the first two terms in the cost function are used (i.e., weights for the rest of the terms being set to zero).

The model adopted for the 3DVAR analysis is the Weather Research and Forecasting (WRF) model configured with a spatial resolution at 2 km, which is run operationally at HKO [14,15]. This 2-km WRF model mainly serves to provide a first guess to the 3DVAR analysis and does not impose a constraint during cost function minimization (the weight of "model" cost function term being set to zero). Pre-processing of the weather radar data has been performed, including removing non-meteorological signals with a correlation coefficient (RhoHV) less than 0.8 and de-aliasing of the Doppler velocities.

The retrieved three-dimensional wind field is produced every 6 min on a grid with spacing of 1 km. Although a 2-km WRF forecast is used as the first guess, the model term is assigned zero weight during cost-function minimization, so the final analysis is constrained primarily by radar radial velocities and mass continuity rather than by the model background. Nevertheless, retrieval quality at low levels may still be affected by radar-beam geometry, velocity de-aliasing uncertainty, and the differing Nyquist velocities and sampling characteristics of the C-, S-, and X-band radars. For this reason, the present study interprets the 1 km level mainly as a low-level diagnostic layer rather than attempting a detailed characterization of fine-scale boundary-layer structure.

It is noted that aspects of the broader approach of combining numerical weather prediction model output with Doppler radar observations for wind retrieval are related to prior intellectual property (e.g., Patent Nos. US9274250B2, WO2022039675A1 and CN113419246B). The present work applies the publicly available PyDDA software package for operational case study evaluation and does not constitute a commercial exploitation of those patents.

4. Comparison with Wind Profiler Data

Independent profiler observations provide a useful operational reference for evaluating radar-derived analyses, especially in regions with complex terrain and heterogeneous low-level flow [16]. HKO operates a boundary-layer type radar wind profiler with a central frequency of 1299 MHz at Sham Shui Po (SSP) in the urban center. This profiler emits electromagnetic waves in three directions (one vertical and two oblique) to measure the three components of the wind by assuming uniform wind within the measurement volume. In non-rainy weather conditions, the three components of the wind are measured from the reflection of the electromagnetic waves by refractive discontinuities in the atmosphere. In rain, the reflection is caused mainly by the falling raindrops and the horizontal winds are tracked by advection of the raindrops by the wind. The vertical velocity in this case is then mainly contributed by the terminal velocity of the raindrops but not the vertical motion of the air. Since the present comparison is mainly made in rainy weather conditions (in which there would be quality return signals for weather radars), only horizontal winds from an SSP wind profiler would be used for the comparison with the weather-radar-based

retrieved wind field, and vertical velocity is not considered. In fact, for the cases under consideration, the "vertical velocity" from the SSP wind profiler is mainly the terminal velocity of the raindrops and does not give positive values, but significant updraft (up to several tens of m/s) is occasionally found in the weather-radar-based retrieved wind field.

The retrieved wind data from multiple weather radars at the nearest grid point to the SSP wind profiler are extracted at various heights, namely, from 1 km to 6 km above sea level, with an increment of every 1 km. Since the C-band radar has not been operated for many episodes of heavy rain, only data in a limited period of time are considered, namely, during the rain events from 27 March to 20 April 2026. For the weather-radar-retrieved wind field, the following horizontal wind data would be removed: (i) having a horizontal speed more than 51.4 m/s, and (ii) radar echoes from fewer than two weather radars are detected. The weather radars in use include: the two S-band radars at Tai Mo Shan and Tate's Cairn, the C-band radar at Cheung Chau, the X-band phased array weather radar at Sha Lo Wan (near HKIA), and two X-band phased array weather radars at Shenzhen (namely, Qiu Yu Tan and Xi Chong). Because X-band radars have lower Nyquist velocities and are more prone to velocity aliasing in intense convection, all Doppler velocities were quality-controlled and de-aliased before the analysis. The locations of these radars are shown in Figure 1. Recent studies have also shown that combining Doppler observations from multiple radars, including systems operating at different wavelengths, can improve the robustness and vertical completeness of three-dimensional wind retrievals [17].

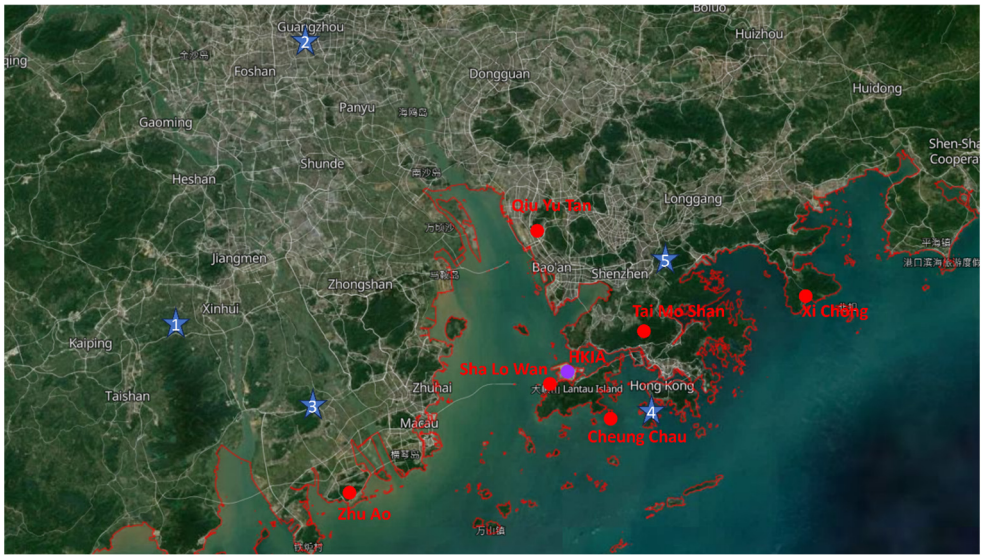

Figure 1. Locations of the weather radars (red circles) used to retrieve the three-dimensional wind field, and locations of the reported hail cases listed in Table 1 (blue stars).

The comparison results are shown in Figure 2, for horizontal wind speed (Figure 2a) and horizontal wind direction (Figure 2b) at all heights in the whole period. The comparison is considered to be satisfactory, namely, the best-fit straight lines have a slope close to unity, and the correlation coefficient required is around 0.9. There are more than 360 data points in each scatter plot. The root-mean-square-difference is about 5.7 m/s for wind speed and 36.4 degrees for wind direction. More data will be accumulated so that comparison results for a much longer period of time will be reported in the literature in the future. It should be noted that the retrieved wind field at 1 km above sea level is primarily used as a low-level diagnostic layer to capture significant wind features such as downdrafts and convergence zones, rather than as a detailed characterization of planetary boundary layer (PBL) structure. The vertical resolution of the retrieval (1 km) limits the ability to

resolve fine-scale PBL processes. Nonetheless, the wind field at this level is found to be in reasonable agreement with the wind profiler observations, lending confidence to its use as a qualitative indicator of low-level wind features associated with intense convective weather.

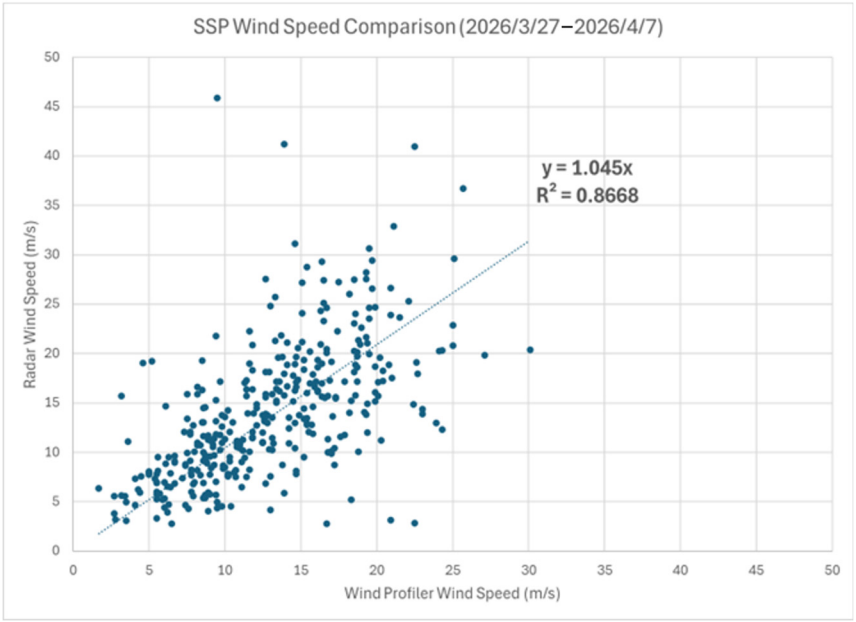

(**a**)

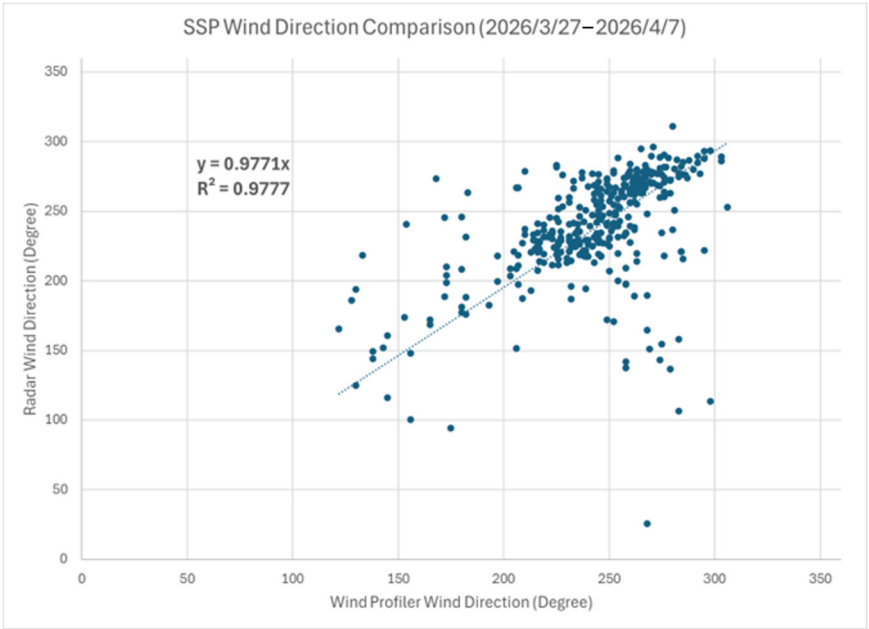

(**b**)

Figure 2. Scatter plot of the radar-derived horizontal wind speed (**a**) and horizontal wind direction (**b**) with the corresponding data at the Sham Shui Po wind profiler.

5. Severe Squall—30 March 2026

On that day, a surface trough was lingering over the inland areas of southern China, whereas the coastal areas, including Hong Kong, are affected by active south to southwesterly winds. A squall line developed over the western coast of Guangdong and moved eastwards, affecting the territory in the late morning at about 10 H local time (02 UTC, with Hong Kong time = UTC + 8 h). The radar reflectivity shows a northeast–southwest-oriented band of echoes approaching the northwestern part of Hong Kong from the northwest

(Figure 3a). The convection is not particularly active and a vertical cross-section across the band of echoes (Figure 3a) shows that the reflectivity reaches a height of about 7 km only. Nonetheless, this rainband is associated with significant squall. Following its approach, a weather station at the northwestern part of Hong Kong, namely, Lau Fau Shan, records a change of 10 min mean wind, namely, from southwesterly winds of about 8 m/s to northwesterly winds of about 15 m/s at around 10 H (Figure 3b for wind speed and Figure 3c for wind direction). Most notable is the occurrence of a very severe gust, namely, the 3 s gust reaches a maximum of 35.6 m/s at about one minute before 10 H, i.e., having hurricane force level. This kind of severe gust may have a significant impact on the Lau Fau Shan area.

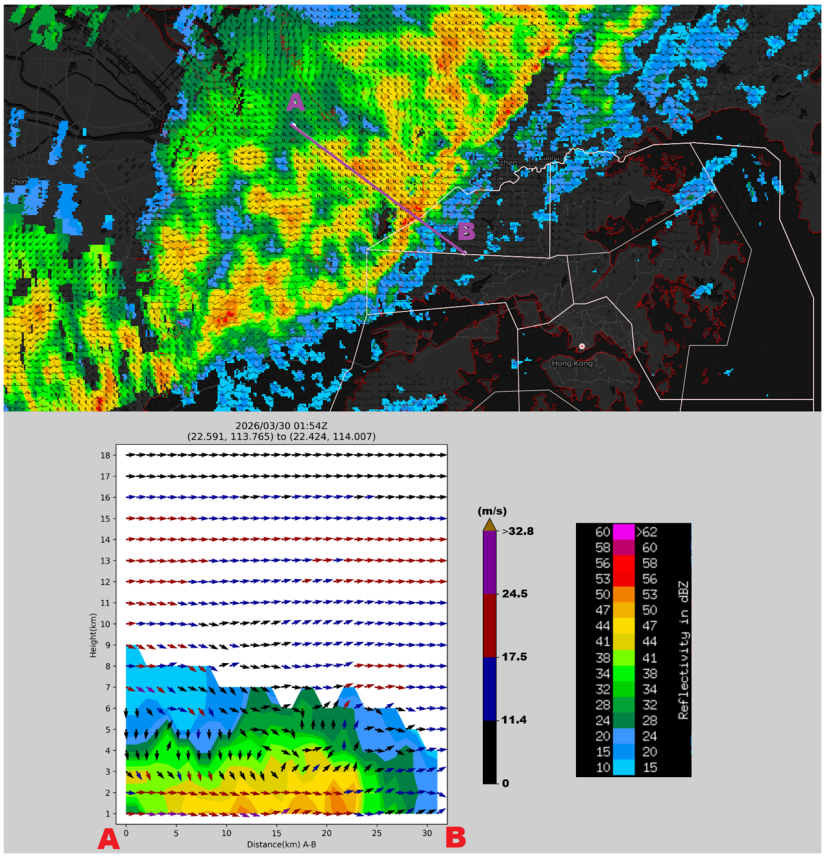

(**a**)

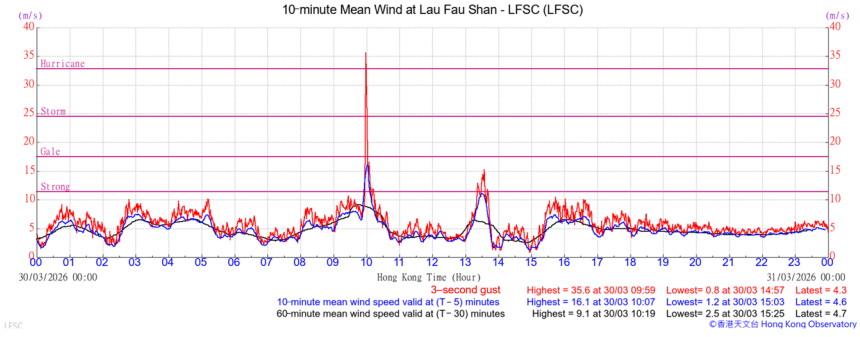

(**b**)

Figure 3. *Cont.*

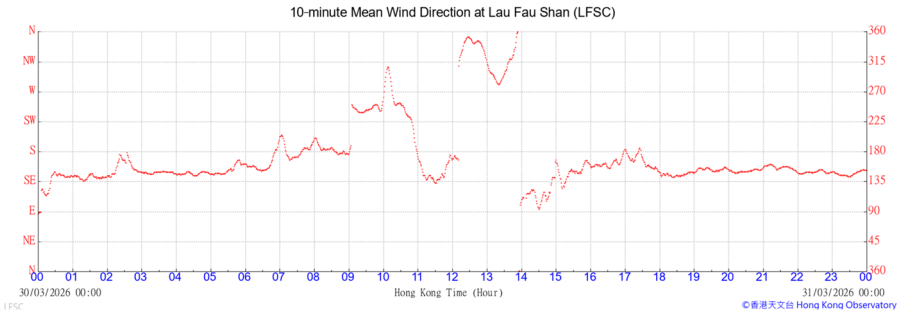

(**c**)

Figure 3. S-band radar reflectivity with 1 km high wind field at 01:54 UTC of 30 March 2026, with vertical cross-section of wind field (**a**) and the time series of wind speed (**b**) and wind direction (**c**) at Lau Fau Shan on 30 March 2026.

The availability of Cheung Chau weather radar data makes it possible to analyze the winds closer to the sea level, namely, at a height of about 1 km, as shown in the inset of Figure 3a. Ahead of the radar reflectivity core, downward motion of the air has been analyzed at a height of 1 km in the three-dimensional wind field, with the component of the wind projected on the cross-sectional plane reaching a wind speed of gale force (wind arrow in brown in the inset of Figure 3a, with a wind speed between 17.5 m/s and 24.5 m/s). The momentum transport associated with such intense downdrafts is an important factor in producing severe surface gusts, as demonstrated in earlier microburst research [18]. Contrary to a mature squall line (e.g., as documented by Chan et al. (2025) [1]), the downdraft seems to originate from a rather shallow layer, namely, from about 2 km above sea level only, with the winds at higher altitude having generally upward motion in the radar reflectivity core. The availability of Cheung Chau weather radar data makes the retrieval of the three-dimensional wind field more complete, and such wind data (at a height of 1 km) would be useful for the advance alerting of significant downdraft near the surface.

6. Orographic Rainfall—6 April 2026

Synoptically, a surface trough lingers over inland areas of southern China and Hong Kong is affected by moderate south to southwesterly winds. The weather was rather convective—as shown in the 00 UTC radiosonde on that day in Hong Kong, K-index is 36 degrees Celsius and convective available potential energy (CAPE) is slightly above 1000 J/kg. Light showers were affecting the territory in the southerly flow, with possible orographic lifting of the winds by the terrain in Hong Kong, as shown in the radar reflectivity imagery (Figure 4a, with the terrain of Hong Kong in the background map). The radar echoes reach a height of about 2 km only and are associated with shallow convection. Though only a limited amount of weather radar data is available, the retrieved wind field shows some interesting features about the vertical motion of the air (Figure 4b), namely, upward motion is generally analyzed in the windward slopes of Hong Kong, e.g., on the western part of Hong Kong for Tai Mo Shan and the mountains on Lantau Island. Such a retrieved wind field can help identify the dynamical mechanisms responsible for terrain-enhanced precipitation, including localized ascent on windward slopes [19].

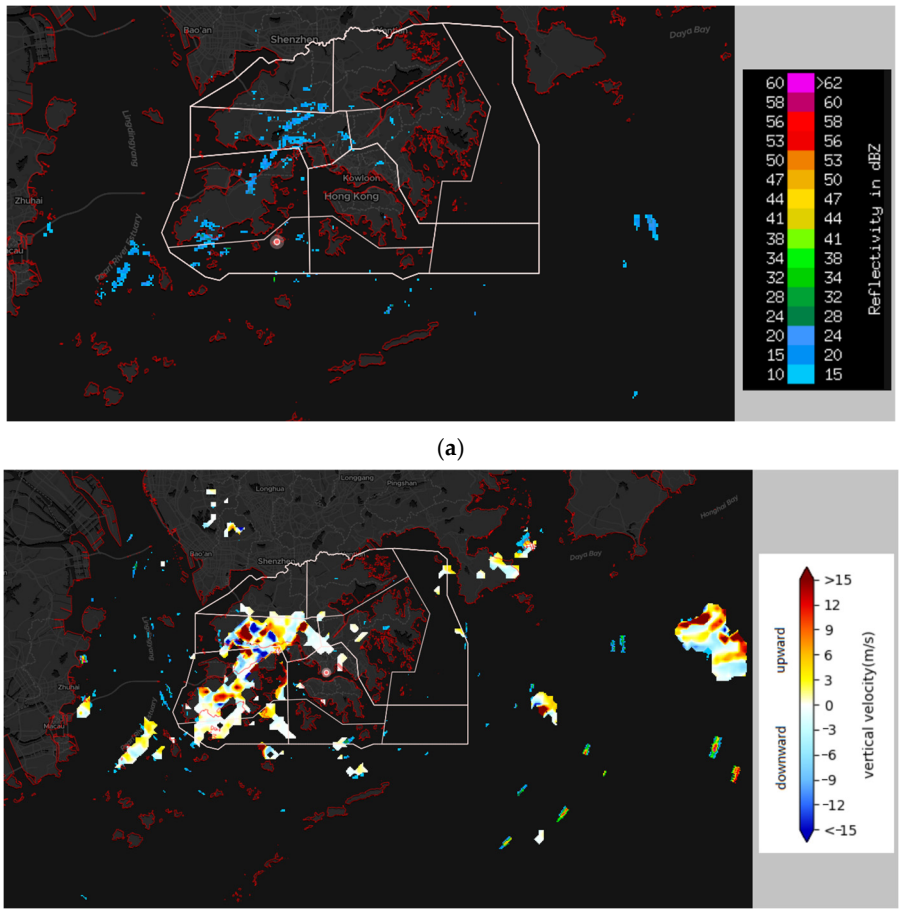

Figure 4. Radar reflectivity (**a**) and the radar-retrieved vertical velocity at a height of 1 km (**b**) showing orographic precipitation.

Lee et al. [20] have analyzed some past orographic rainfall cases in Hong Kong and found that it may be related to the moist Froude number and the 0 to 900 m wind speed for the southwesterly wind regime, following the regime diagram as determined from numerical experiments in [21]. Based on the results of [20], orographic rainfall is considered to be possible on that day using the 00 UTC radiosonde of Hong Kong on 6 April 2026. This is consistent with the radar reflectivity observations and the weather-radar-retrieved wind field. Again, without the Cheung Chau weather radar, it is not possible to retrieve the winds as low as 1 km above sea level and thus to confirm the occurrence of orographic rainfall. This is consistent with recent studies showing that low-level radar observations are particularly valuable for identifying shallow orographic precipitation processes and for improving precipitation analysis over complex terrain [22].

7. Suspected Hail and Meso-Vortex—5 April 2026

The surface trough over the northern part of the South China Sea is only located at about 1 degree of latitude south of Hong Kong on that day and is moving gradually towards the coast. Under the influence of the surface trough, together with troughing flow at 850 hPa and short waves in the mid-tropospheric westerlies, the weather is very unstable over south China coastal areas. From the 00 UTC radiosonde in Hong Kong on 5 April 2026, the K-index is about 33 degrees Celsius and the parameters relating to meso-vortex occurrence such as Significant Tornado Parameter (SigTor) and Supercell composite parameter (SCP) according to [23] have climatologically rather high values of 0.83 and 2.50. The Storm Relative Helicity (SRH) also has a rather high value of 293 m^2/s^2. Both

the dynamic and thermodynamic conditions are favorable for the occurrence of significant convection in the vicinity of Hong Kong.

In the late morning (around 1030H, Figure 5a), the hydrometeor classification of Tai Mo Shan radar gives an extensive and strong signal of hail occurrence near Dangan Island to the south of Hong Kong. However, there is limited habitation on that island. The hail occurrence cannot be confirmed with independent eyewitness reports. Around that time (e.g., about 1130 H, Figure 5b), Hong Kong is still "protected" by easterly winds from the surface weather station observations but there is significant convergence between the easterly and southeasterly winds to the south of Hong Kong from the ocean radar's wind observations whose quality has been established following the study of [24], favoring the occurrence of intense convection in that region. It is interesting to note that, over the offshore waters of eastern Guangdong, the ocean radar gives anticyclonic flow at the surface, and there is no convective activity over that area as confirmed with the occurrence of nil weather radar echoes (Figure 5b).

A vertical cross-section is cut across the major weather radar echo near Dangan Island at about 02:30 UTC (Figure 6a). The echo core has a reflectivity of more than 60 dBZ (purple in color in Figure 6a). The freezing level has a height of about 5 km above sea level on that day based on radiosonde data of Hong Kong. The vertical cross-section shows a clear signature of overhanging echoes, with the reflectivity exceeding 60 dBZ above the freezing level, which is a clear signature for the occurrence of hail. This interpretation is consistent with modern hail-detection approaches that relate strong radar signatures to storm thermal structure, including the height of relevant isotherms and the vertical distribution of intense reflectivity [25]. From the weather-radar-retrieved wind field, there is a significant updraft in the elevated region of 60 dBZ reflectivity, indicating intense convection and the strong updraft helps to support the growth of hailstones. At a later time (Figure 6b), the overhanging echo persists but descends to a lower altitude, namely, the elevated 60 dBZ reflectivity has descended from a height of about 6 km to 4 km above sea level. But it is still associated with a significant updraft. The rainband appears to be weakening a bit, but should still be bearing hail.

With the gradual retreating of surface easterly winds, the convective activity over the sea spreads to the north gradually. To the southwest of Hong Kong, intense echo (with reflectivity exceeding 60 dBZ) appears to move towards the western part of the territory at about 05:12 UTC (Figure 7a). However, compared with the convection near Dangan earlier on that day, this region of convection appears weaker and reaches a height of about 9 km only. But there is still a signature of overhanging echo from the vertical cross-section (inset of Figure 7a). The air motion within the radar reflectivity core is mainly downdraft, and no significant updraft could be identified. Though it is weaker, it is interesting to note that, at a height of 4 km above sea level, the vertical velocity field shows interlacing upward and downward motion from the northeast to southwest direction (Figure 7b). The convection appears to be associated with some kind of mid-tropospheric wavy motion, possibly gravity waves.

At around that time (about 05:22 UTC), about 150 km to the south of Hong Kong, the Cheung Chau weather radar depicts an inverted-V shape radar echo in its 0.8-degree PPI scan (Figure 8a) with a clear signature of mesoscale vortex (Figure 8b). By using all the available weather radar data, the retrieved wind field shows a cyclonic circulation with a size of about 100 km at a height of 2 km above sea level (Figure 8c). A vertical cross-section is made across this cyclonic circulation and the resulting wind field is shown in the inset of Figure 8c. Significant updraft is found near the center of this meso-cyclone all the way up to a height of 18 km (the upper bound of the analysis domain), whereas downdraft is analyzed to the southwest of it at the location of the stronger reflectivity on its southern

periphery. From the signature of radar reflectivity, occurrence of cyclonic circulation in the lower troposphere and the significant upward motion near the center, the system appears to be a supercell, which is not commonly found in the northern part of the South China Sea in early Spring.

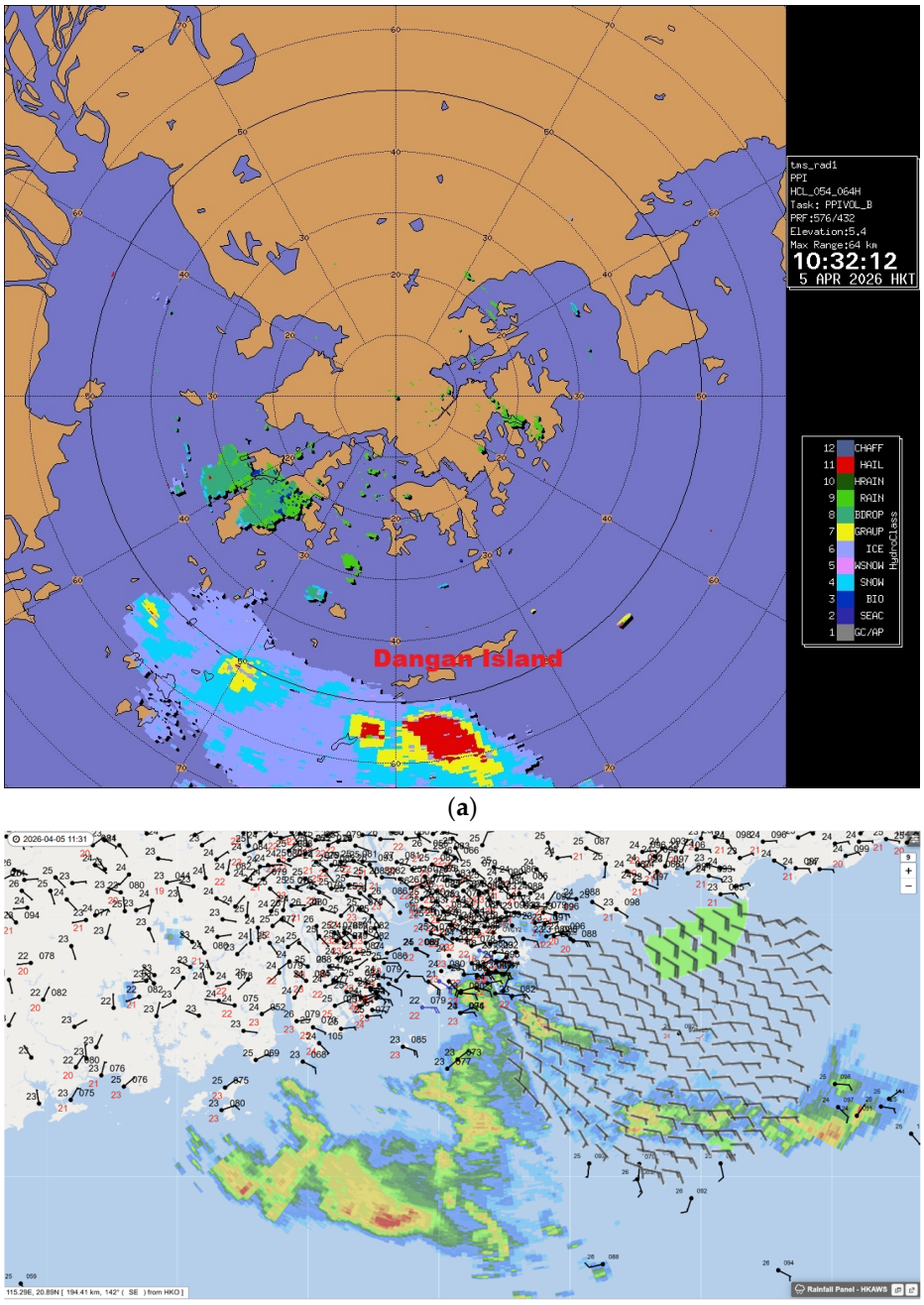

Figure 5. Hydrometeor classification from Tai Mo Shan weather radar (**a**), showing a strong signature of hail (red); (**b**) shows the radar echoes, surface weather observations (wind barbs with black dots) and winds from the ocean radar over the sea (wind barbs without black dots). The dew point temperatures and the dry-bulb temperatures are in degree Celsius.

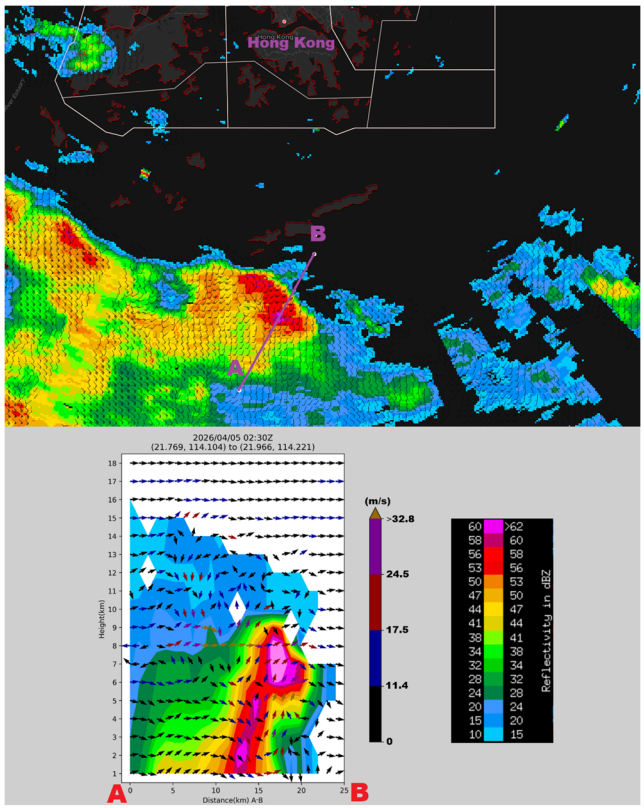

(**a**)

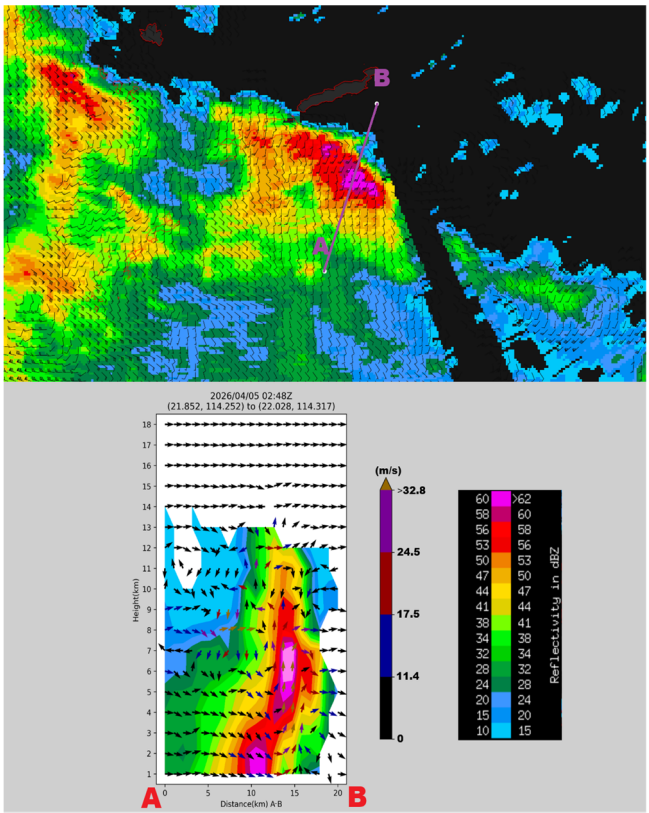

(**b**)

Figure 6. The radar echoes and 1 km wind field at 02:30 UTC (**a**) and 02:48 UTC (**b**) on 5 April 2026, with the vertical cross-sections across the intense echoes at Dangan Island.

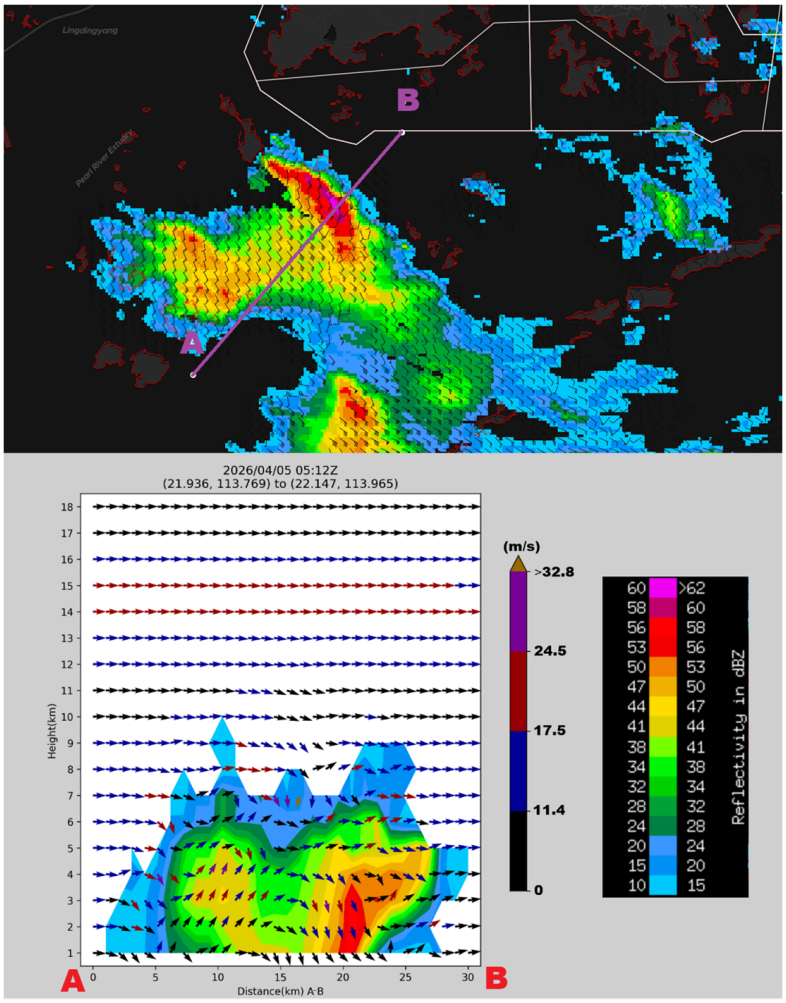

(**a**)

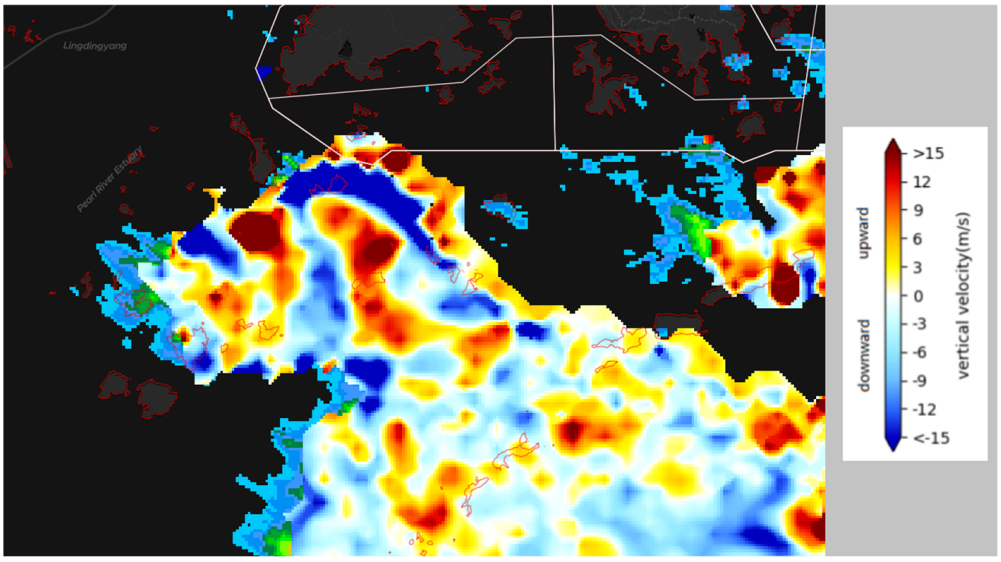

(**b**)

Figure 7. The radar reflectivity at a height of 1 km showing the strong echo to the southwest of Hong Kong at 05:12 UTC on 5 April 2026 (**a**) and the corresponding radar-retrieved vertical velocity at a height of 4 km (**b**).

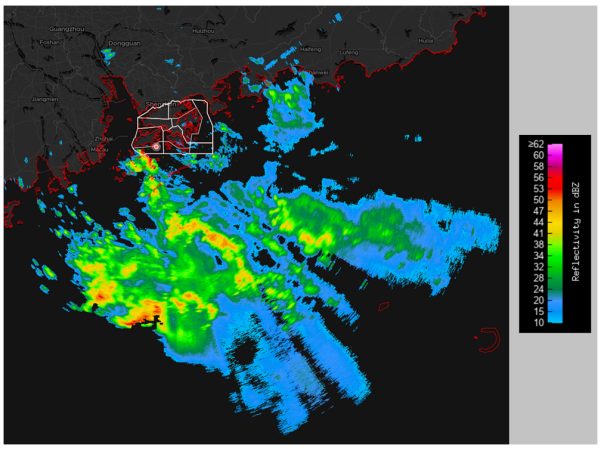

(**a**)

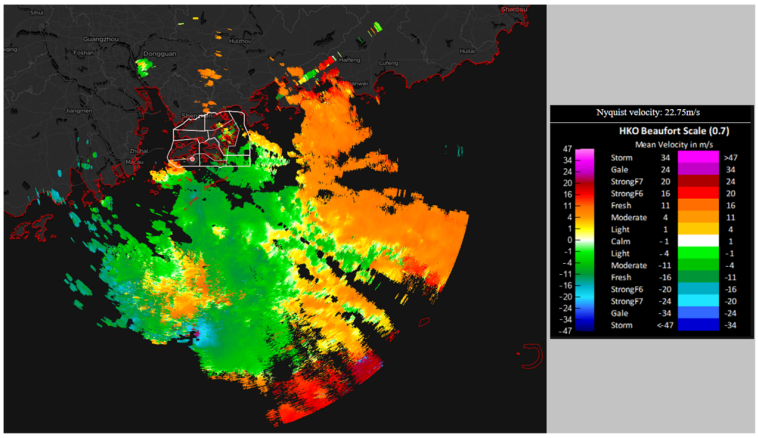

(**b**)

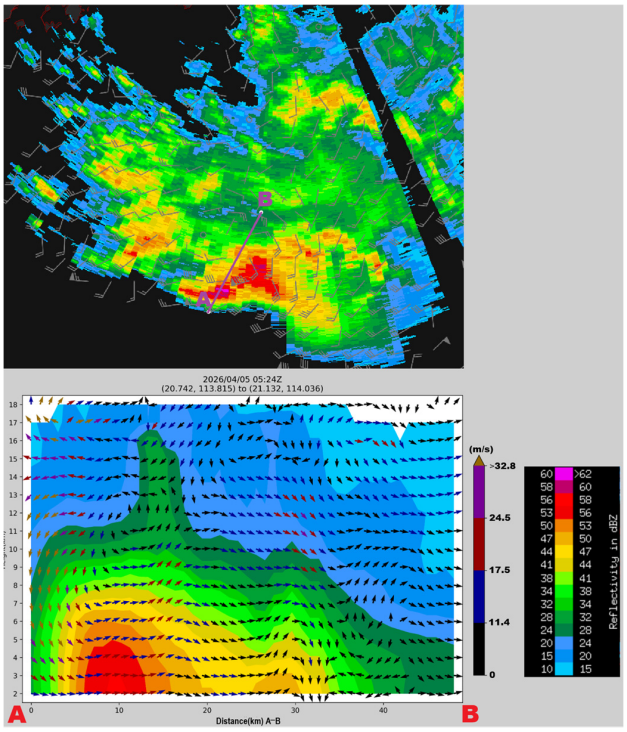

(**c**)

Figure 8. Radar reflectivity (**a**) and Doppler velocity (**b**) from Cheung Chau weather radar for the suspected supercell to the south of Hong Kong, with the vertical velocity across the cyclonic circulation (**c**) at around 05:24 UTC on 5 April 2026.

8. Hail, Squall and Micro-Vortex—17 April 2026

A surface trough moves southwards across the coast of southern China later on that day, resulting in unstable weather in the Pearl River Estuary in the evening. This type of organized convective wind event is also meteorologically relevant in South China, where recent climatological work has documented bow-echo occurrence under regional warm-season convective environments [26]. Before the occurrence of the intense convective weather in Hong Kong, radiosonde ascent data are available in the territory at 00 UTC and 06 UTC of 17 April 2026. SigTor is found to be 0.12 to 0.18, and SCP is found to be 0.32 to 0.48. Both appear to be rather low values. SRH is 50.0 m^2/s^2 and 40.7 m^2/s^2 respectively, also relatively low. CAPE is found to increase from 530 to 974 J/kg, and K-index also rises from 28.5 to 35.2 degrees Celsius in this 6 h period. The atmosphere is found to be increasingly unstable following the approach of the surface trough, but meso-cyclone, tornado or supercell may not be expected.

Significant convection first appears over the western coast of Guangdong. More detailed analysis was made of the radar echoes associated with a number of hail reports at Doumen, Zhuhai, on the western coast of Pearl River Estuary at about 07 UTC (15H local time), with the hail size in the region of 2 mm to 20 mm. At around that time (06:48 UTC, Figure 9a), the 1 km high wind field shows convergence between the northerly winds behind the surface trough and the southerly winds from the sea, resulting in a significant updraft up to 18 km (inset of Figure 9a). About 48 min later (Figure 9b), the convection has intensified with a stronger reflectivity core (more than 60 dBZ) and significant updraft inside up to 18 km (inset of Figure 9b). The vertical cross-section also shows an overhanging echo, which is consistent with the reports of hail. The hydrometeor classification at 06:50 UTC (14:50H) shows that there could be graupel/hail, rain/hail or hail in the region (left hand side of Figure 9c) and the hail size estimate based on [27] gives a value mostly in the region of 15 to 20 mm, with some pixels reaching 20 to 25 mm (right-hand side of Figure 9c), which is consistent with the ground observations.

The development zone of convection then extends further eastwards to affect the eastern coast of the Pearl River Estuary, including Hong Kong. Intense squalls have been reported by a number of weather stations over the territory. The rainband first affects HKIA and then moves east to southeastwards across Hong Kong. Hail was reported at Lamma Island (location in Figure 10a) at about 08:44 UTC (16:44H local time). Hail size was not reported in the news, but according to the videos available on the internet, it was in the order of a few mm to 10 mm. The intense convection then continues to move east. The associated squalls have brought about some damage, as reported in the news (e.g., from The Standard, https://www.thestandard.com.hk/news/article/329640/Strong-winds-bring-down-scaffolding-and-trees-in-Ap-Lei-Chau-3-hurt, accessed on 12 June 2026). At 16:54 H local time, scaffolding with a size of 20 m by 30 m had fallen at Ap Lei Chau (location in Figure 10a), hurting three persons. Around 20 min later, the strong winds caused the collapse of a tree in the same district. Two trees were broken; one fell on a car parked on the road and broke the glass of the car. A driver in that district also heard the noise of some solid materials hitting the car's top, suspecting that there might be hail but could not confirm it. The convection gradually weakens and departs from Hong Kong afterward.

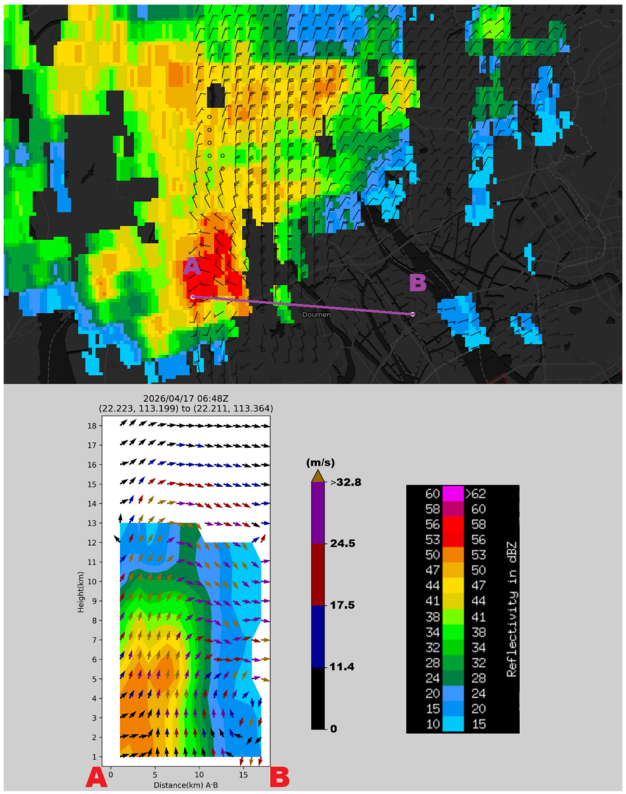

(**a**)

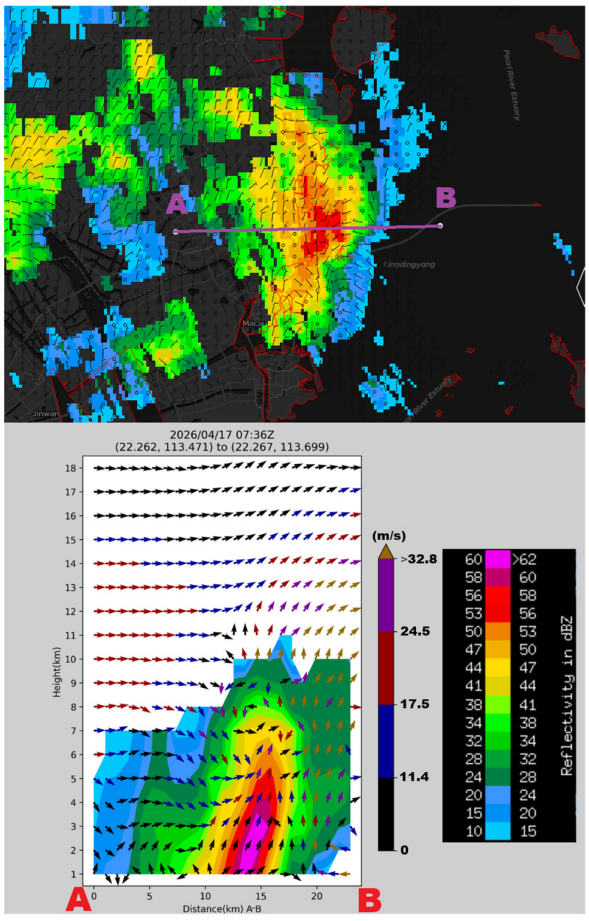

(**b**)

Figure 9. *Cont.*

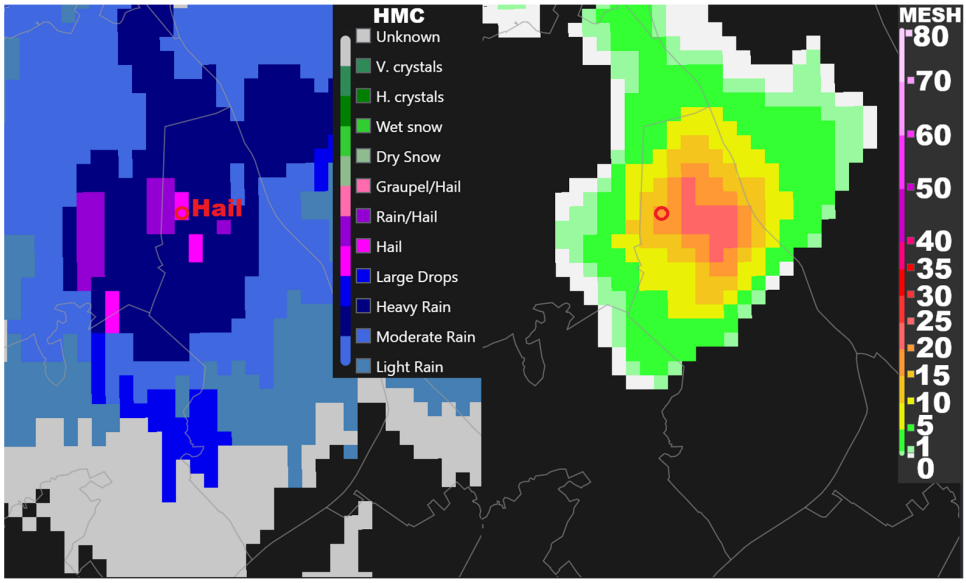

(**c**)

Figure 9. Radar reflectivity and wind field for the hailstorm at Zhuhai (**a**) at 06:48 UTC and 07:36 UTC on 17 April 2026 (**b**), and the hydrometeor classification (HMC) (left) and Maximum Estimated Size of Hail (MESH) (right) from Cheung Chau radar (**c**).

The radar picture in Figure 10a shows the rainband crossing the Victoria Harbour of Hong Kong at about 08:30 UTC, taking the form of a bow echo. Bow echoes are well known to be efficient producers of severe downdraft, and their development is commonly associated with organized convective systems capable of generating strong low-level outflow and damaging gusts [28,29]. There is a significant downdraft from a height of 5 km to 1 km ahead of the reflectivity core, consistent with the observation of squalls by the weather stations at that time. For instance, at the location of Star Ferry with the Harbour, the 10 min mean wind increases from a few m/s to about 10 m/s with the wind direction remaining west to northwesterly (time series of wind speed and wind direction in Figure 10b and Figure 10c respectively). The 3 s gust reaches a maximum of 15.7 m/s.

About 12 min later, the rainband starts to affect Lamma Island, remaining in the form of a bow echo (Figure 11a). In the vicinity of Lamma Island, the Doppler velocity imagery of Cheung Chau radar shows that there is a micro-scale vortex (Figure 11b). Previous radar and damage analyses of severe bow echoes have shown that embedded vortices can locally enhance destructive surface winds, which is consistent with the above-mentioned reported damage [30]. Small-scale vortical circulations have also been discussed in urbanized environments, although the present case is interpreted primarily in association with the bow-echo circulation rather than with urban heat-island forcing [31,32]. A vertical cross-section is made across the radar reflectivity core (Figure 12a). Between 1 km and 4 km, there is a significant downdraft, probably associated with the squalls and the falling of hail. At the same time, updraft is still seen between 4 km and 10 km with an overhanging radar echo, showing that the convection remains active. Occurrence of hail is possible at that time. Six minutes later (Figure 12b), the rainband moves eastwards and is affecting Ap Lei Chau. The vertical cross-section across the reflectivity core does not show a sign of significant updraft, indicating that the convection is weakening. Nonetheless, overhanging radar echo is still observed, and the occurrence of hail over Ap Lei Chau is possible, though not confirmed by ground observations.

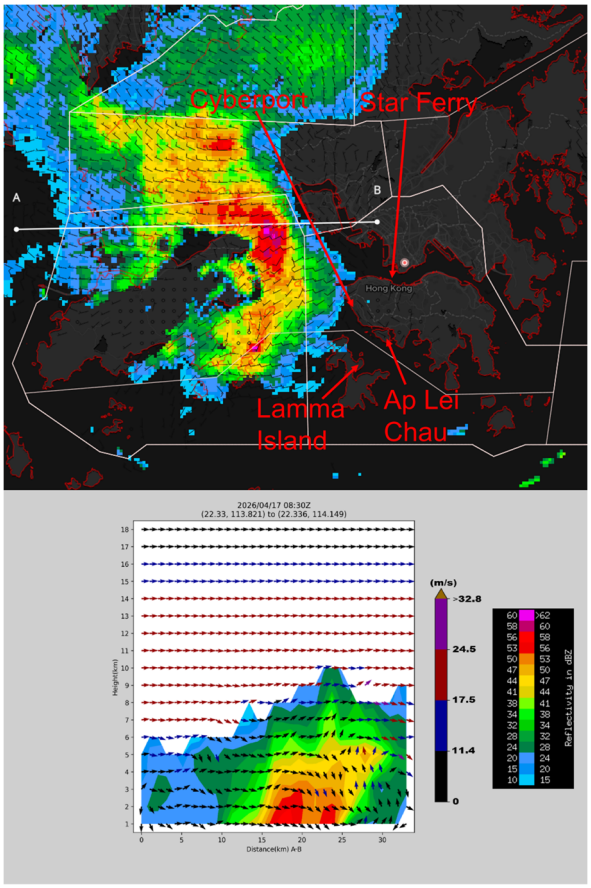

(**a**)

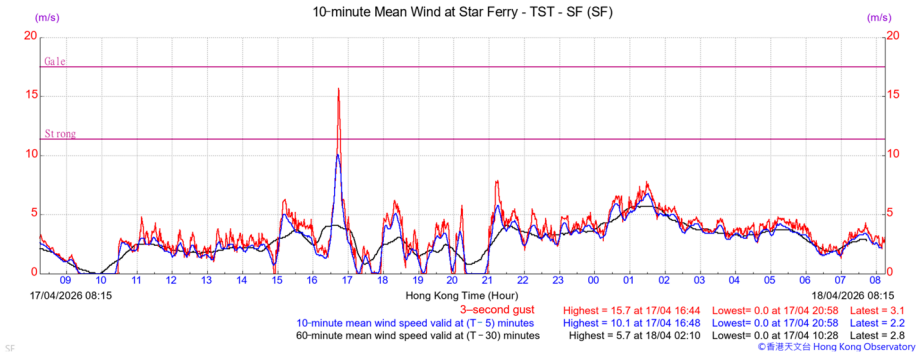

(**b**)

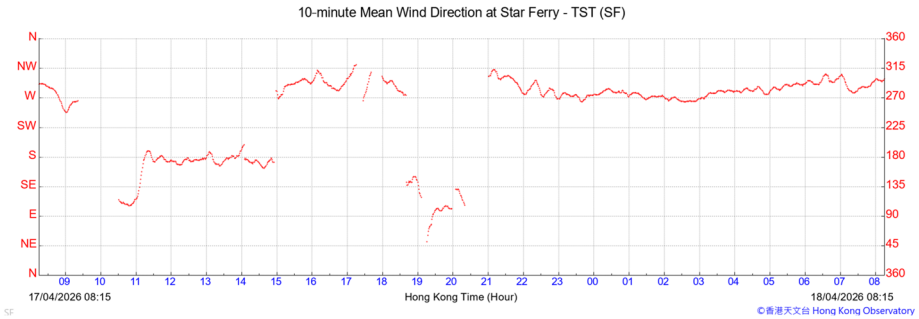

(**c**)

Figure 10. The bow echo crossing Victoria Harbour at 08:30 UTC on 17 April 2026 (**a**) and the time series of wind speed (**b**) and wind direction (**c**) at Star Ferry.

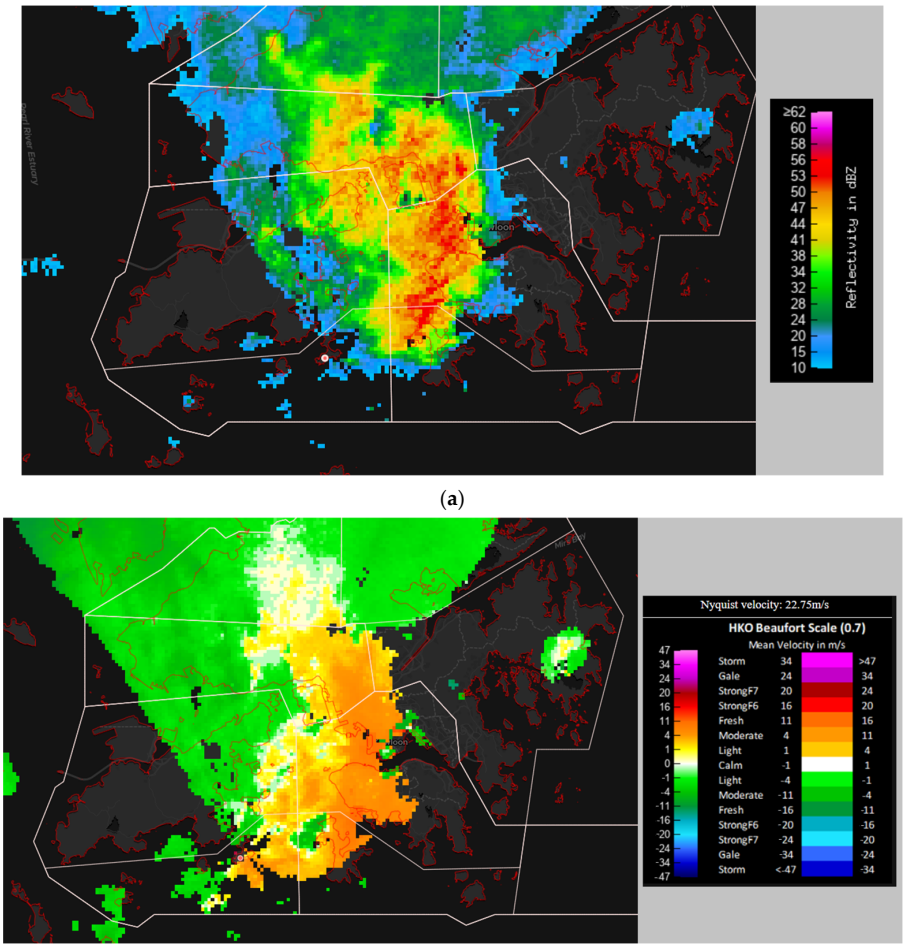

Figure 11. The 1.4-degree PPI reflectivity (**a**) and Doppler velocity (**b**) from Cheung Chau radar at 08:42 UTC on 17 April 2026 when the bow echo reaches Lamma Island, showing the micro-scale vortex.

Figure 13 shows the hydrometeor classification (HMC) at 500-m altitude and Maximum Estimated Size of Hail (MESH) at ground level from three consecutive volume scans of the Cheung Chau weather radar, namely, 08:40 UTC (Figure 13a), 08:45 UTC (Figure 13b) and 08:50 UTC (Figure 13c) on 17 April 2026. There is an extensive area of rain/hail or hail in association with the bow echo, gradually moving eastwards. At 08:45 UTC (at a time closest to the report time), near the locations of Lamma Island and Ap Lei Chau Island, the MESH values range from 1 mm to 20 mm, with the 95th-percentile value falling in the 5–10 mm category, consistent with eyeball estimation based on a video provided by the spotter.

During the event of convective weather on 17 April 2026, a vertically scanning light detection and ranging (LIDAR) system is working at Cyberport (location in Figure 10a). The time–height plot of vertical wind profiles from this LIDAR is shown in Figure 14. Only 10 min mean wind is available from this LIDAR, and it is found to reach strong force (wind barb in blue) to gale force (wind barb in red) between a height of 200 m and 700 m above ground during the passage of the bow echo, which is consistent with the three-dimensional wind field as retrieved by the weather radars. This LIDAR serves to provide real-time wind data for supporting low-altitude economy (LAE) using unmanned aerial systems (UAS). Significant squalls, as demonstrated in this case, have great impact on the operation of UAS, and a weather radar scanning at low altitudes, as in the case of Cheung Chau weather radar, is crucial to support LAE.

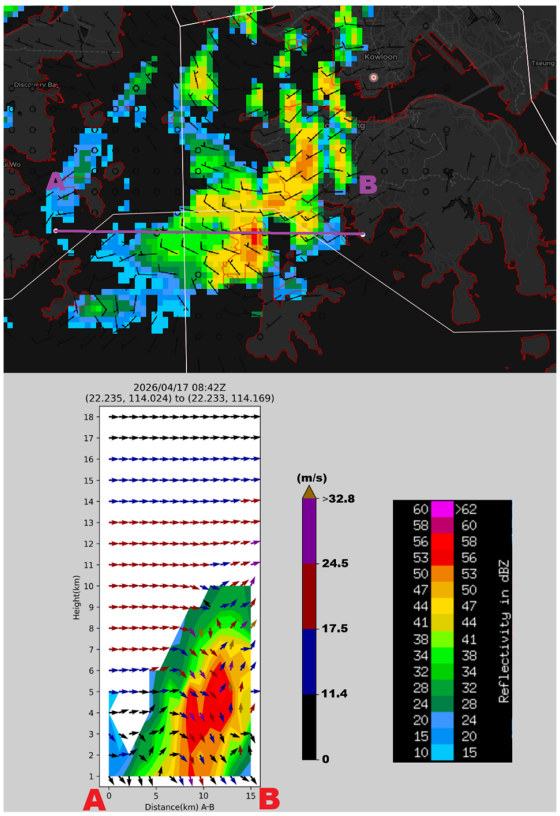

(**a**)

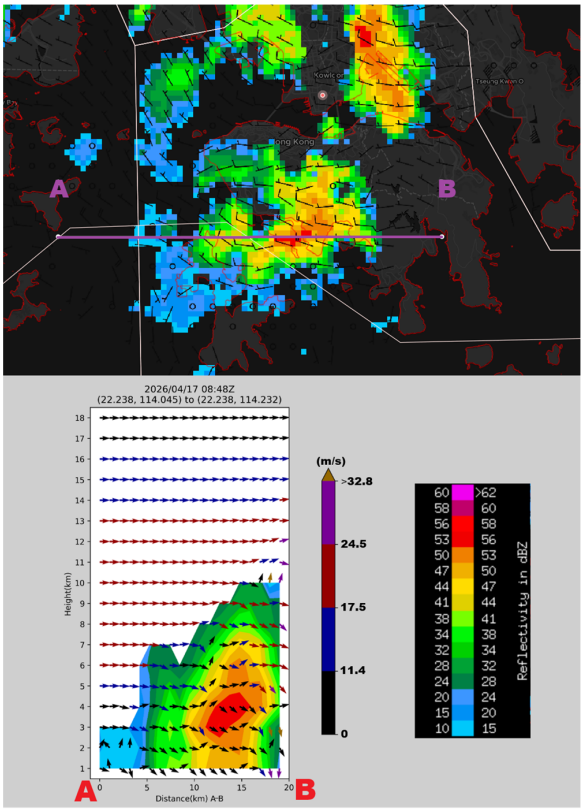

(**b**)

Figure 12. 1 km high S-band radar reflectivity with wind field with vertical cross-sections of the hail-bearing storm at Lamma Island at 08:42 UTC (**a**) and at Ap Lei Chau at 08:48 UTC (**b**) on 17 April 2026.

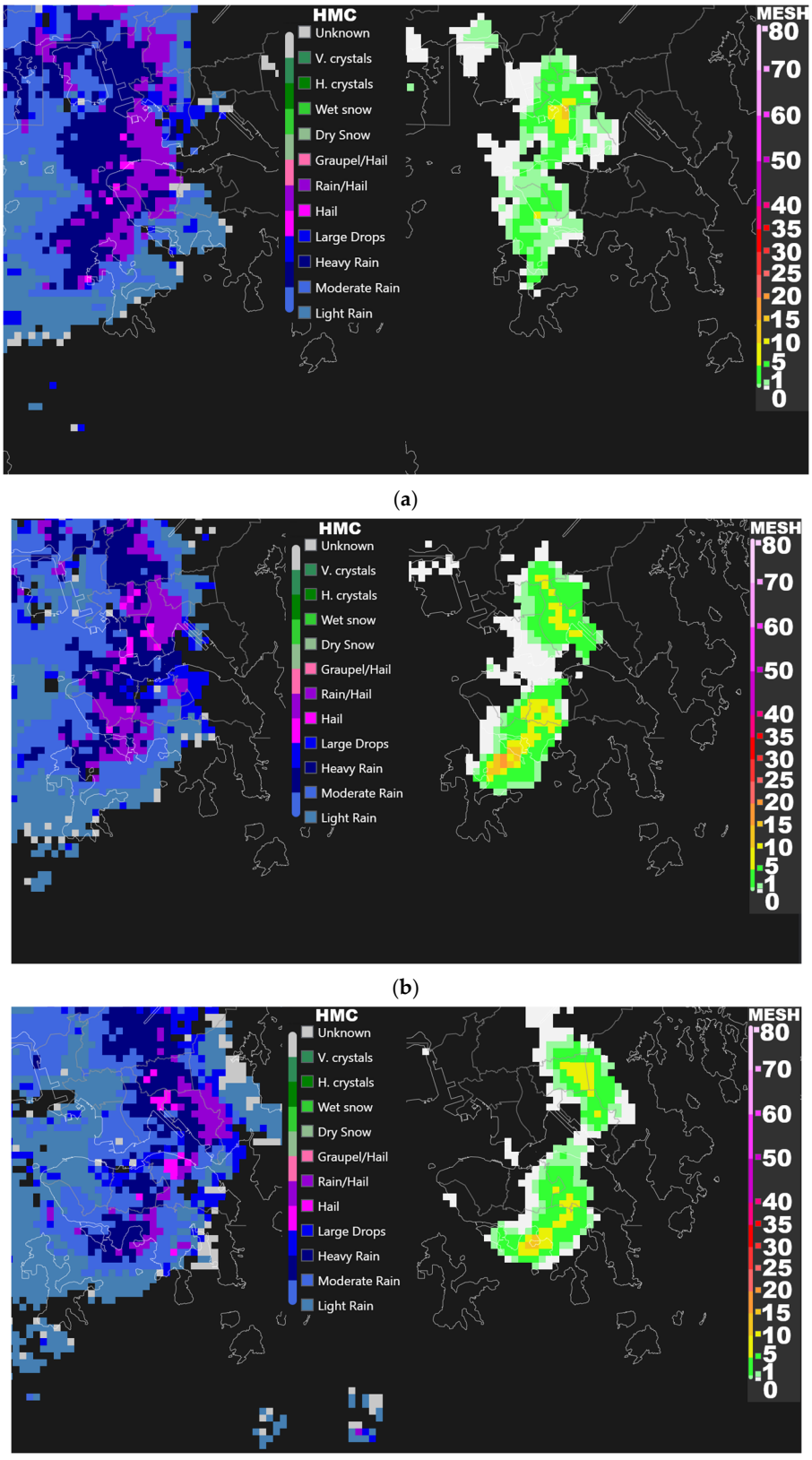

Figure 13. The HMC at 500 m altitude (left) and MESH (right) valid on 17 April 2026. Panels (**a**–**c**) refer to observation times at 08:40 UTC, 08:45 UTC and 08:50 UTC respectively. Legends for HMC and MESH are magnified and shown in the right column. The MESH is in units of millimeters (mm) and displayed as categorized colors: light green/gray for <1 mm, green for 1–5 mm, yellow for 5–10 mm, orange-yellow for 10–15 mm, orange for 15–20 mm, etc.

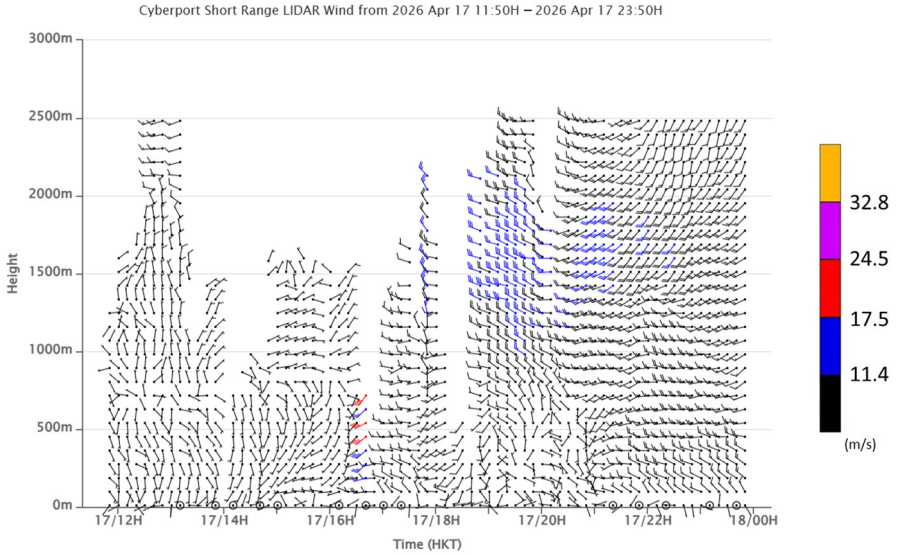

Figure 14. The time-height cross-section of the vertical wind profile measured by the LIDAR at Cyberport. Data with values less than 0.1 m/s are depicted as circles.

9. Comparison of Radar-Estimated Hail Size with Actual Observations

Since the start of the trial run of the Cheung Chau weather radar in February 2026, there are a number of hail cases reported/suspected over the Pearl River Estuary cities in March and April 2026. Hail size reports are available for some of the events, with five of them located within the detection range of Cheung Chau weather radar. Table 1 lists all the five hail cases, namely four reported cases (Case 1 to 4) with significant hail sizes and one "nil report" case in Shenzhen (Case 5). The real-time HMC and MESH products for calculating the expected maximum hail size are displayed in Figures 13b and 15a–d.

Table 1. Comparison between the reported hail size and the estimated maximum size of hail from the Cheung Chau weather radar. The radar hail size corresponds to the MESH-derived hail-size category at an analysis time chosen to be as close as possible to the reported hail time.

Case	Date	Time (LST)	City	District	Hail Size (mm)	
					Reported	Radar
1	27 March 2026	14:00	Jiangmen	Xinhui	5–8	5–10
2	29 March 2026	15:00	Guangzhou	Liwan/Yuexiu	5–8	5–10
3	17 April 2026	15:00	Zhuhai	Doumen	~20	15–20
4	17 April 2026	16:42	Hong Kong	Lamma Island	~10	5–10
5	20 April 2026	14:10	Shenzhen	Luohu	nil	<1

As summarized in Table 1, the maximum hail sizes calculated based on HMC/MESH (see next paragraph for details), at a time chosen to be as close as possible to the reported hail occurrence, verify favorably against the reported hail sizes to within the same categories for all the five cases. The "nil report" in Case 5 is considered consistent with the expected very small hail of size less than 1 mm. Hail of such small size could actually be either melted or not noticed on reaching the ground. For Case 2, the reported hail location is beyond 100 km from the Cheung Chau site and low-altitude HMC is not directly available from the Cheung Chau weather radar. The hail classification shown in Figure 15b corresponds to a height of about 8.4 km. This case is still counted as a "hit" because low-altitude HMC from the S-band dual-pol weather radar at Tai Mo Shan does confirm hail classification around

that location. However, as seen in Figure 13, the MESH field can change noticeably within a few minutes, so the categorization in Table 1 should be interpreted as a representative snapshot rather than a time-averaged estimate.

Given the uncertainty associated with HMC/MESH and in order to reduce false alarms, the following processing steps are applied before making a comparison with the reported hail sizes:

(i) select only those locations (pixels) that are classified as hail, rain/hail or graupel/hail at low altitudes well below the freezing level (which is climatologically well above 4 km in the spring season in the region of interest);
(ii) over the selected locations, rank the corresponding MESH distribution;
(iii) calculate the 95th-percentile MESH value as the expected maximum hail size;
(iv) categorize the resulting 95th-percentile value into the following bins: <1 mm, 1–5 mm, 5–10 mm, 10–15 mm, 15–20 mm, etc. (as shown in the lower legend in Figure 13).

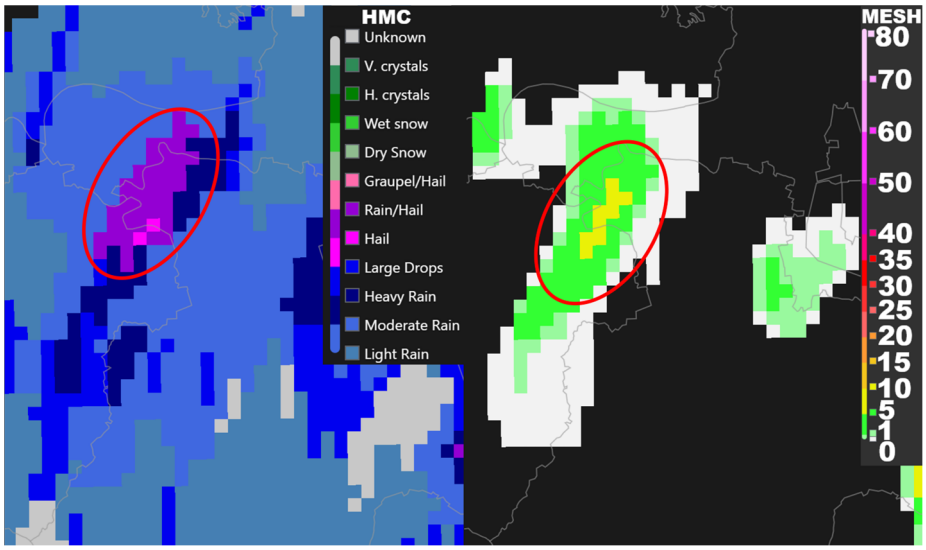

(**a**)

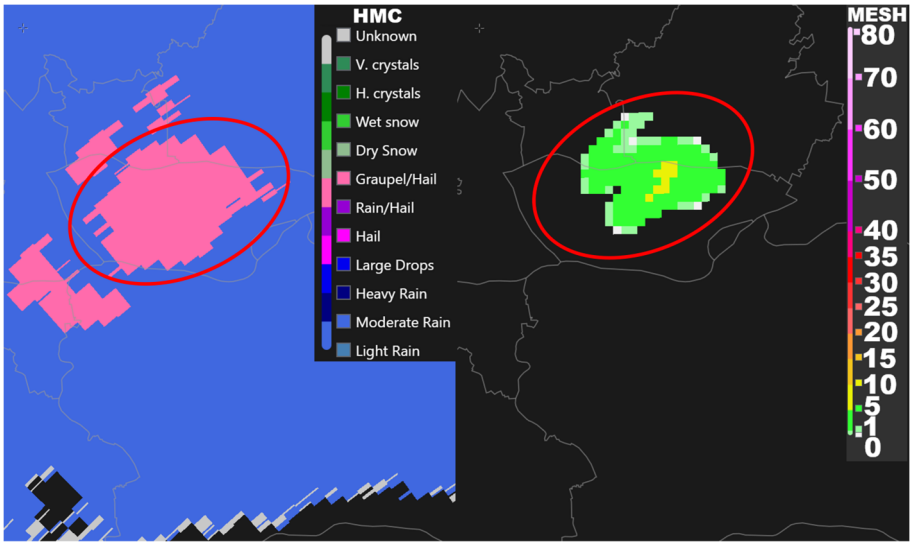

(**b**)

Figure 15. *Cont.*

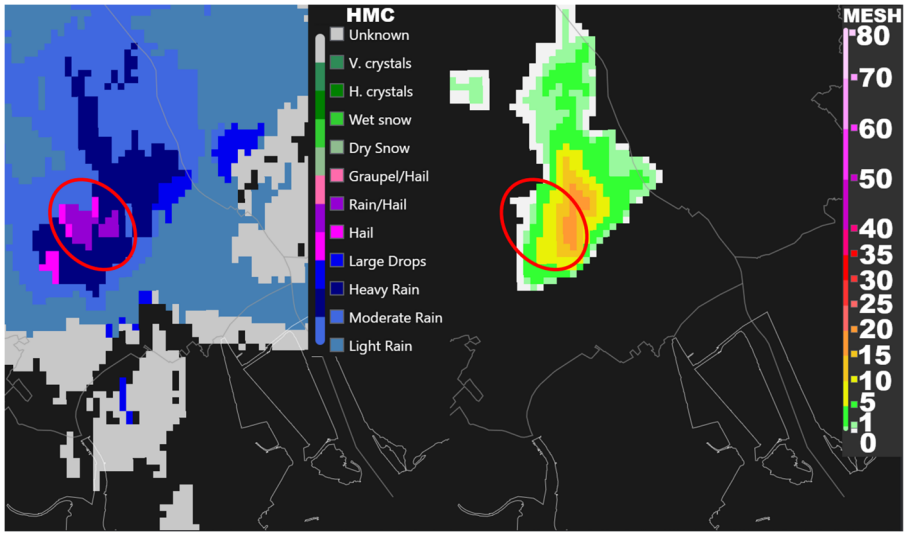

(**c**)

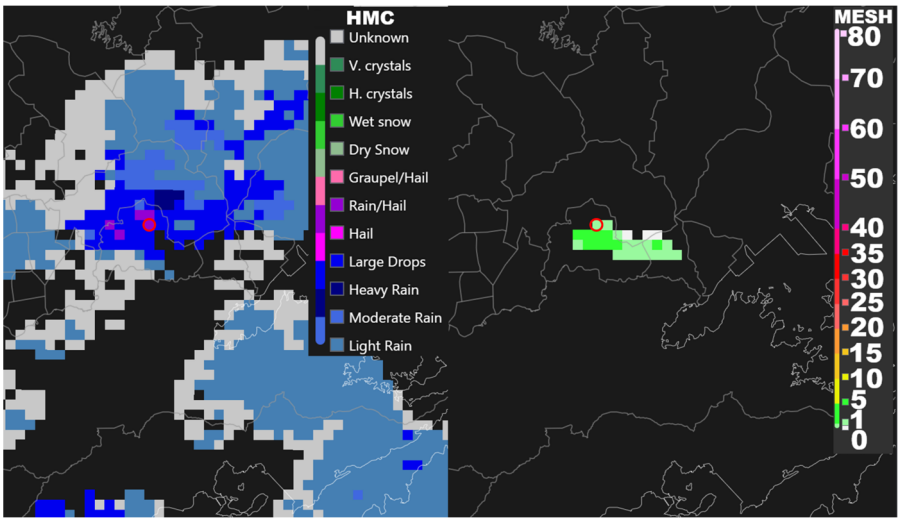

(**d**)

Figure 15. The low-altitude HMC (left) and MESH (right) images for the hail cases in Table 1. (**a**) Case 1 in Jiangmen on 27 March; (**b**) Case 2 in Guangzhou on 29 March; (**c**) Case 3 in Zhuhai on 17 April; and (**d**) Case 5 in Shenzhen on 20 April 2026. Legends are the same as those in Figure 13. The red lines highlight the locations of hail, rain/hail or graupel/hail. (Note: the HMC in (**b**) is from a PPI scan at 3.5-degree elevation, about 8.4 km high).

10. Conclusions

The Cheung Chau C-band solid-state weather radar has been on a trial run for a few months only. Its lower scanning altitude is found to significantly supplement the existing S-band surveillance weather radars in the analysis of intense convective weather in Hong Kong, a coastal city with hilly terrain. This paper focuses on two major applications of this radar, namely, analysis of the wind field in the atmospheric boundary layer (1 km above sea level) and detection of hail (through comparison with ground reports) through case studies. Though the number of cases is limited in a statistical sense, the radar shows the potential to significantly enhance the understanding and alerting of intense convective weather, such as squalls associated with rainbands, orographic precipitation, and hail alerting with possible provision of estimated maximum hail size in the alerting messages. More cases will be accumulated in the coming years in order to build up a larger database for studying the usefulness of this radar and tuning the performance of hail detection. Moreover, its

observations in other kinds of severe weather, notably tropical cyclones, are yet to be seen and tested.

Due to the hilly terrain of Hong Kong, there are still a number of blind spots under the surveillance of the Cheung Chau radar. Though there is a plan to set up a network of X-band phased array weather radars in the Pearl River Estuary, their rapid attenuation in heavy rain limits the monitoring and alerting capabilities of severe weather to a certain extent. On the other hand, a network of C-band weather radars with less power consumption may appear to be a more workable approach to addressing the issue of monitoring the atmospheric boundary layer, at least for Hong Kong itself. Further installation of similar radars over the territory is still subject to more prolonged study, e.g., on the reliability of this kind of technology, on the observation capability for various kinds of severe weather over the coast of southern China, and on the technology of integrating their data together with those from the existing radars for enhancing the nowcasting of intense convective weather in Hong Kong. These aspects will be reported in future papers.

Author Contributions: Conceptualization, P.-W.C.; methodology, H.Y.Y. and P.-W.C.; software, T.-K.L. and K.K.L.; validation, T.-K.L.; formal analysis, T.-K.L., K.K.L. and P.-W.C.; investigation, T.-K.L.; resources, H.Y.Y.; data curation, T.-W.H.; writing—original draft, T.-K.L., H.Y.Y. and P.-W.C.; supervision, H.Y.Y. and P.-W.C.; project administration, H.Y.Y. and P.-W.C. All authors have read and agreed to the published version of the manuscript.

Funding: This research received no external funding.

Institutional Review Board Statement: Not applicable.

Informed Consent Statement: Not applicable.

Data Availability Statement: The data presented in this study are available on request from the corresponding author.

Conflicts of Interest: The authors declare no conflicts of interest.

References

1. Chan, P.-W.; Chan, Y.-W.; Cheung, P.; Chong, M.-L. An observational study of a severe squall line crossing Hong Kong on 15 March 2025 based on radar-retrieved three-dimensional winds and flight data. *Appl. Sci.* **2025**, *15*, 8562. [CrossRef]
2. Brandes, E.A. Gust front evolution and tornado genesis as viewed by Doppler radar. *J. Appl. Meteorol.* **1977**, *16*, 333–338. [CrossRef]
3. Ray, P.S.; Ziegler, C.L.; Rasmussen, E.N.; Wilson, J.W. Single- and multiple-Doppler radar observations of tornadic storms. *Mon. Weather Rev.* **1980**, *108*, 1607–1625. [CrossRef]
4. Kropfli, R.A.; Hildebrand, P.H. Three-dimensional wind measurements in the optically clear planetary boundary layer with dual-Doppler radar. *Radio Sci.* **1980**, *15*, 283–296. [CrossRef]
5. Hane, C.E.; Wilhelmson, R.B.; Gal-Chen, T. Retrieval of thermodynamic variables within deep convective clouds: Experiments in three dimensions. *Mon. Weather Rev.* **1981**, *109*, 564–576. [CrossRef]
6. Pasken, R.; Lin, Y.-L. Pressure perturbations within a tornadic storm derived from dual-Doppler wind data. *Mon. Weather Rev.* **1982**, *110*, 1555–1574.
7. Li, J.; Chen, Y.-L.; Lee, W.-C. Analysis of a heavy rainfall event during TAMEX. *Mon. Weather Rev.* **1997**, *125*, 1060–1082. [CrossRef]
8. Zhang, G.; Mahale, V.N.; Putnam, B.J.; Kumjian, M.R.; Cao, Q.; Reeves, H.D.; Ryzhkov, A.V.; Xue, M.; Wu, D.; Zhang, P.; et al. Current status and future challenges of weather radar polarimetry bridging the gap between radar meteorology–hydrology–engineering and numerical weather prediction. *Adv. Atmos. Sci.* **2019**, *36*, 571–588. [CrossRef]
9. Forcadell, V.; Augros, C.; Caumont, O.; Dedieu, K.; Ouradou, M.; David, C.; Figueras i Ventura, J.; Laurantin, O.; Al-Sakka, H. Severe-hail detection with C-band dual-polarisation radars using convolutional neural networks. *Atmos. Meas. Tech.* **2024**, *17*, 6707–6734. [CrossRef]
10. Jackson, R.; Collis, S.; Lang, T.; Potvin, C.; Munson, T.; Pydda, A. A Pythonic direct data assimilation framework for wind retrievals. *J. Open Res. Softw.* **2020**, *8*, 20. [CrossRef]
11. Shapiro, A.; Potvin, C.K.; Gao, J. Use of a vertical vorticity equation in variational dual-Doppler wind analysis. *J. Atmos. Ocean. Technol.* **2009**, *26*, 2089–2106. [CrossRef]

12. Gao, J.; Xue, M.; Shapiro, A.; Droegemeier, K.K. A variational method for the analysis of three-dimensional wind fields from two Doppler radars. *Mon. Weather Rev.* **1999**, *127*, 2128–2142. [CrossRef]
13. Potvin, C.K.; Shapiro, A.; Xue, M. Impact of a vertical vorticity constraint in variational dual-Doppler wind analysis: Tests with real and simulated supercell data. *J. Atmos. Ocean. Technol.* **2012**, *29*, 32–49. [CrossRef]
14. Wong, W.-K.; Lau, C.-S.; Chan, P.-W. Aviation model: A fine-scale numerical weather prediction system for aviation applications at the Hong Kong International Airport. *Adv. Meteorol.* **2013**, *2013*, 532475. [CrossRef]
15. Hon, K.-K. Tropical cyclone track prediction using a large-area WRF model at the Hong Kong Observatory. *Trop. Cyclone Res. Rev.* **2020**, *9*, 67–74. [CrossRef]
16. Chen, H.; Cifelli, R.; White, A. Improving operational radar rainfall estimates using profiler observations over complex terrain in Northern California. *IEEE Trans. Geosci. Remote Sens.* **2020**, *58*, 1821–1832. [CrossRef]
17. Tsai, C.-L.; Kim, K.; Liou, Y.-C.; Lee, G. Advantages of using multiple Doppler radars with different wavelengths for three-dimensional wind retrieval. *Atmos. Meas. Tech.* **2025**, *18*, 6371–6392. [CrossRef]
18. Lin, Y.-L.; Coover, W.E. Momentum and eddy kinetic energy transports by a multiple microburst-producing storm. *J. Geophys. Res. Atmos.* **1990**, *95*, 7625–7640. [CrossRef]
19. Cheng, L.-W.; Yu, C.-K.; Chen, S.-P. Identifying mechanisms of tropical-cyclone-generated orographic precipitation with Doppler radar and rain gauge observations. *npj Clim. Atmos. Sci.* **2025**, *8*, 35. [CrossRef]
20. Lee, F.Y.; Woo, W.C.; Leung, Y.Y. Case study of orographic rainfall in Hong Kong. In Proceedings of the 29th Meteorological Technical Seminar of Guangdong, Hong Kong and Macao, Macao, China, 20–22 January 2015.
21. Chu, C.-M.; Lin, Y.-L. Effects of orography on the generation and propagation of mesoscale convective systems in a two-dimensional conditionally unstable flow. *J. Atmos. Sci.* **2000**, *57*, 3817–3837. [CrossRef]
22. Mandapaka, P.V.; Germann, U.; Panziera, L. Diurnal cycle of precipitation over complex Alpine orography: Inferences from high-resolution radar observations. *Q. J. R. Meteorol. Soc.* **2013**, *139*, 1025–1046. [CrossRef]
23. Leung, Y.T.; Lam, K.F.; Lau, T.K.; Chan, Y.W.; Chan, P.-W. Meteorological indices for potential occurrence of waterspout/tornado in Hong Kong. *Meteorol. Z.* **2025**, *34*, 81–91.
24. Hui, D.; Lam, C.-C.; Chan, P.-W.; Huang, C.; Yang, S. Enhancements of an ocean radar system for improved wind observations in weather monitoring operations. *Appl. Sci.* **2026**, *16*, 3497. [CrossRef]
25. Pilorz, W.; Zięba, M.; Szturc, J.; Łupikasza, E. Large hail detection using radar-based VIL calibrated with isotherms from the ERA5 reanalysis. *Atmos. Res.* **2022**, *271*, 106185. [CrossRef]
26. Zhou, A.; Zhao, K.; Xu, X.; Liu, Q.; Ding, Z.; Huang, H.; Liu, X.; Rao, X.; Hu, S. A climatological study on the two types of bow echoes over South China. *J. Geophys. Res. Atmos.* **2023**, *128*, e2023JD038720. [CrossRef]
27. Witt, A.; Eilts, M.D.; Stumpf, G.J.; Johnson, J.T.; Mitchell, E.D.; Thomas, K.W. An enhanced hail detection algorithm for the WSR-88D. *Weather Forecast.* **1998**, *13*, 286–303. [CrossRef]
28. Weisman, M.L. The genesis of severe, long-lived bow echoes. *J. Atmos. Sci.* **1993**, *50*, 645–670. [CrossRef]
29. Johns, R.H. Meteorological conditions associated with bow echo development in convective storms. *Weather Forecast.* **1993**, *8*, 294–299. [CrossRef]
30. Wheatley, D.M.; Trapp, R.J.; Atkins, N.T. Radar and damage analysis of severe bow echoes observed during BAMEX. *Mon. Weather Rev.* **2006**, *134*, 791–806. [CrossRef]
31. Chiao, S.; Pasken, R. Surface mesovortices formation and maintenance in the St. Louis metropolitan area. *Meteorol. Appl.* **2006**, *13*, 21–37. [CrossRef]
32. Mainhart, B.D.; Niyogi, D.; Pasken, R.; McGrath, K.; Davis, A. Surface mesovortices in relation to the urban heat island effect over the Saint Louis metropolitan area. *Urban Clim.* **2020**, *34*, 100695. [CrossRef]

Disclaimer/Publisher's Note: The statements, opinions and data contained in all publications are solely those of the individual author(s) and contributor(s) and not of MDPI and/or the editor(s). MDPI and/or the editor(s) disclaim responsibility for any injury to people or property resulting from any ideas, methods, instructions or products referred to in the content.